Local Piston Theory as an Alternative to Mesh Deformation: Slender Wing-Body Configurations

Marius-Corné Meijer[1]
University of Pretoria, Pretoria, 0081, South Africa

Laurent Dala[2]
Northumbria University, Newcastle-Upon-Tyne, NE1 8ST, United Kingdom

The suitability of local piston theory (LPT) for modelling static loads on a deforming, low aspect-ratio wing in the presence of aerodynamic interference is investigated. Predictions using Euler-based LPT are compared to Euler solutions for the deformed geometry. Moderate to large deformations are investigated for the leeside wing on a cruciform wing-body configuration. It is shown that LPT is suitable even for large deformations, with the perturbation downwash-Mach number supersonic, provided that the loading induced by deformation is not dominated by interaction with body-vortices or other sources of aerodynamic interference. Second-order LPT is recommended for deformations producing downwash-Mach numbers approaching sonic. The influence of the choice of piston-theory coefficients is in producing an estimation band for the LPT load prediction, with insignificant influence on the load-slope in the present investigation. In conclusion, LPT is put forward as a viable alternative to mesh deformation towards reduction of the computational cost of aerodynamic load prediction for static aeroelasticity, provided that perturbation loads are dominated by local twist and not by vortex interaction.

---

[1] Graduate Research Assistant, Department of Mechanical and Aeronautical Engineering

[2] Head of Mechanical Engineering, Department of Mechanical and Construction Engineering

I. Introduction

Aeroelastic analysis, though typically conducted to verify the structural integrity of the flight vehicle, may be viewed with a focus on the aerodynamic input to the multidisciplinary system. Studies of aerodynamic parameter variation for a given structure are an inherent part of aeroelastic studies, which typically results in aerodynamic modelling being the computationally most expensive component of the analysis. Computational cost is managed through the use of lower-order aerodynamic models with simplified physics. An illustration of the range of methods available is given in Table 1. High-fidelity analysis using computational fluid dynamics (CFD) is typically not suitable for design studies due to the high computational cost. However, the aerodynamic complexity of certain geometries and flight conditions may make the use of CFD unavoidable – particular examples include hypersonic vehicles and reusable booster systems.

Table 1: Example of spectrum of aerodynamic models used in aeroelastic analysis.

Method	Computational Cost	Discretization Required	Physics
Modified Strip Theory [1]	Low	N/A: Analytical method	Linear potential
Vortex-Lattice Method [2]	Medium	Surface: steady panel method	Linear potential
Doublet-Lattice Method [3, 4]	Medium	Surface: unsteady panel method	Linear potential
Euler (steady) + LPT [5]	Medium-High	Volume: computational / analytical	Nonlinear inviscid
Euler (unsteady)	High	Volume: finite volume method	Nonlinear inviscid

A number of cost-reduction strategies are available when the use of CFD is required. These may be loosely grouped into two categories. The first consists of approaches which aim to create a reduced-order model (ROM) of the aerodynamic system without modifying the underlying equations or physics. The development of methods in this category is an active field of research [6] with diverse methods available, such as proper orthogonal decomposition [7], Kriging surrogates [8], and dynamic mode decomposition [9]. These methods typically require a reference set of computational results (“snapshots”) from which to construct the model, and are referred to as *a-posteriori* model order reduction methods. Methods which do not require a reference set of solutions are also available, such as such as proper generalized decomposition [10, 11], and are referred to as *a-priori* ROMs.

The generation of the reference set is computationally expensive, while the construction of the ROM itself is significantly cheaper. This category is therefore suitable when a large number of parameter variations within a bounded parameter space is required.

The second category encompasses methods which aim to reduce the computational cost of each simulation individually. This is achieved either through numerical techniques to accelerate convergence of the solution of the equations, or through simplification of the underlying physics and its mathematical representation. Examples of simplified models include the transonic small-disturbance equations [12], hypersonic small-disturbance equations [13], various approximations to the Navier-Stokes (N-S) equations [14], and local piston theory [5].

An important facet of CFD for aeroelastic analysis is the treatment of the displacement of the fluid boundary due to structural deformation. The structural deformation may either be treated as a physical displacement, leading to mesh deformation, or as prescribing an additional downwash distribution at the boundary of a static mesh – this is known as a transpiration boundary condition [15]. The disadvantage of allowing mesh deformation is the additional computational cost incurred in solving for the mesh displacement; this is particularly significant in problems of dynamic aeroelasticity. While the use of a transpiration boundary condition foregoes the computational expense of mesh deformation, it is prone to degradation in accuracy for moderate to large structural deformations of geometries with aerodynamic interference [16].

Local piston theory (LPT) has seen increasingly wide application with CFD towards providing accurate aerodynamic modelling in problems of dynamic aeroelasticity, with computational cost reduced by an order of magnitude [5, 17] relative to unsteady CFD. The method achieves this cost reduction through simplification of the underlying physics; the 3D partial differential equations for a field are replaced by point-wise algebraic equations at the boundary. Applications of LPT in literature have typically been restricted to simple geometries such as airfoils [5, 18, 19], panels, low aspect-ratio wings [5], or wave-riders [19], and have primarily been concerned with dynamic aeroelasticity. Research into the application of LPT in interfering flows has been sparse, focusing on shock impingement on deforming plates [20, 21]. The application to wing-body configurations [20, 22] has similarly been sparse, with no attention given to the effect of interference on the accuracy of

LPT. A recent application [23] has seen LPT being used in a design optimization study of a wing, with aerodynamic variations due to geometric changes to the baseline configuration being modelled using LPT.

The objective of the work is to investigate the suitability of Euler-based local piston theory in modelling static aerodynamic loads on a wing-like structure subject to aerodynamic interference. The roles of perturbation magnitude and the order of piston-theory applied are also considered.

II. Methodology

A. Geometry and Structure

A cruciform wing-body geometry in the "+" configuration is considered, with the body geometry described in Fig. 1. The body has a total length of 19 calibers, with a 3-caliber tangent-ogive nose. The body geometry was chosen for the experimental and numerical data available [24] on it. The wing geometry is detailed in Fig. 2(a). Each wing has a panel aspect ratio of 1.5; the diameter-to-span ratio for the wing-body combination is 0.33. A wing thickness of 0.5mm was used to isolate thickness effects in the aerodynamic loading. A Young's modulus of 73.1×10^9 Pa, density of $2780\,\mathrm{kg\,m^{-3}}$, and Poisson's ratio of 0.33 were used. The first three natural frequencies of the wing with a description of the modes and their deflections are given in Table 2; the mode-shapes are shown in Fig. 2(b) and Fig. 3 with the maximum displacement amplitude normalized to 10 mm for each mode. Nominal modal deformations of $\delta = 5$ mm and $\delta = 10$ mm are considered, where δ is the magnitude of the maximum displacement on the wing for the given mode shape. These are moderate to large displacements, and were chosen in order to investigate the interaction with the body-shed vortex, which is located approximately 25 mm from the undeformed plane of the wing.

Table 2: Natural modes.

			% Tip deflection		Tip twist [°]	
Mode	Frequency [Hz]	Description	$\delta = 5\,\mathrm{mm}$	$\delta = 10\,\mathrm{mm}$	$\delta = 5\,\mathrm{mm}$	$\delta = 10\,\mathrm{mm}$
1	72.43	First bending	6.0	12	-0.5	-1.0
2	298.4	First torsion	0.45	0.91	-12.3	-23.5
3	403.8	Second bending	-5.6	-11	-1.4	-2.7

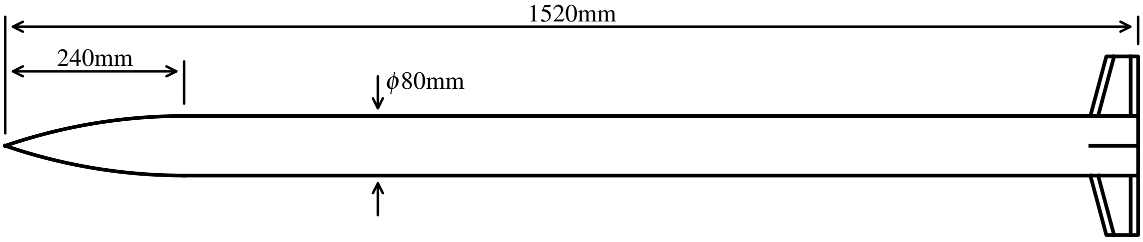

Fig. 1: Body geometry definition.

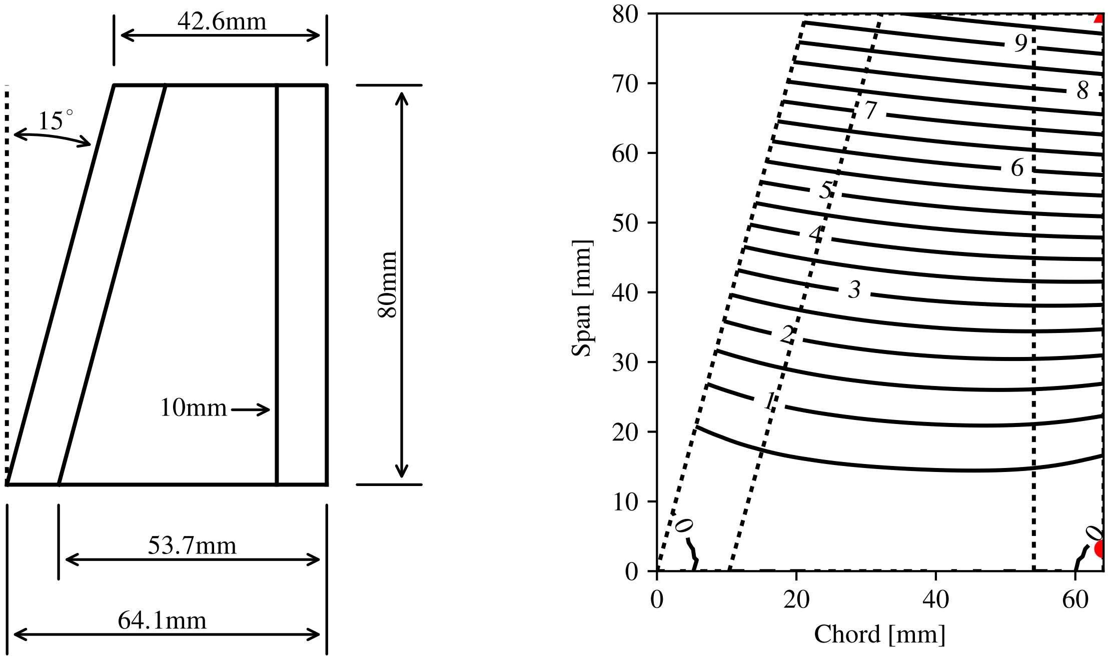

(a)

(b)

Fig. 2: Displacement [mm]: (a) Wing geometry definition; (b) mode 1 (first bending) displacement [mm]. Deflection into the page is defined as positive and is denoted by solid contours.

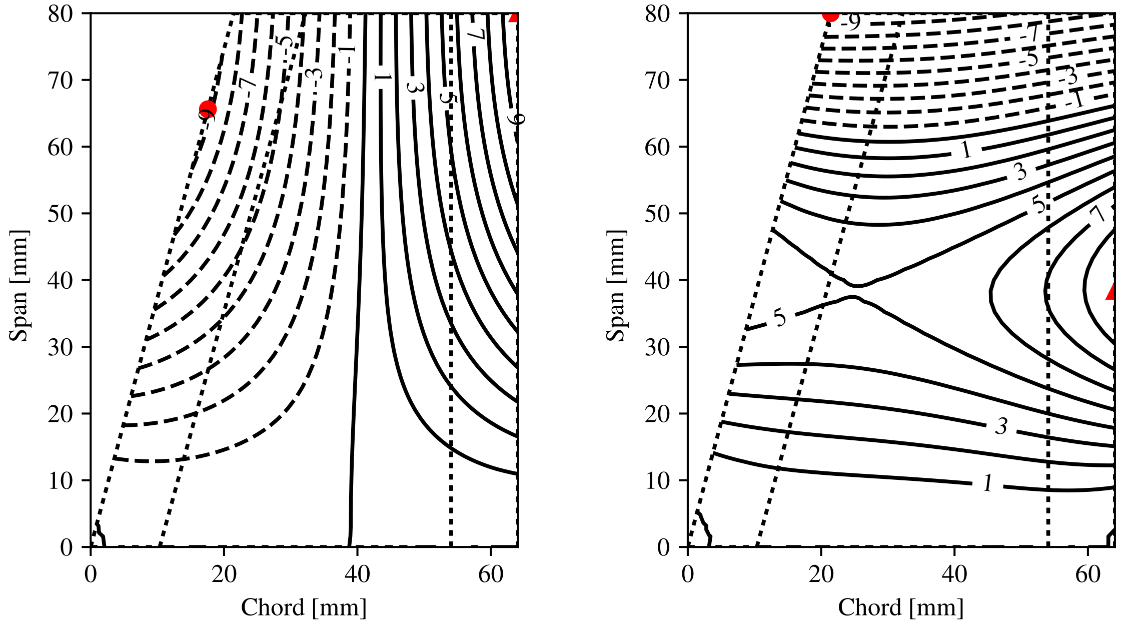

(a)

(b)

Fig. 3: Displacement [mm]: (a) mode 2 (first torsion), (b) mode 3 (second bending). Deflection into the page is defined as positive and is denoted by solid contours.

B. Aerodynamic Modelling

The aerodynamic loading on the leeside wing under a range of flow conditions and deformations is the chief quantity of interest in the present investigation. The parameter space is defined by $2 \leq M_\infty \leq 3$ and $0° \leq \alpha \leq 10°$, where $M\infty$ is the freestream Mach number and α is the angle-of-attack. The freestream conditions of [24] are used and are kept constant over the parameter space, with $P_{0\infty} = 129{,}000\,\text{Pa}$, $T_{0\infty} = 288\,\text{K}$, and $\gamma = 1.4$, where $P_{0\infty}$ is the freestream stagnation pressure, $T_{0\infty}$ is the freestream stagnation temperature, and γ is the ratio of specific heats. The same reference lengths have been used for the loading coefficients as by [24], with $L_{ref} = d = 80\,\text{mm}$, $S_{ref} = \pi d^2/4$, and with the moment reference centre being located at the mid-length of the body ($x_{ref} = 9.5d$). The nomenclature for the loading coefficients is defined in Fig. 4.

The steady flowfield for both undeformed and deformed geometries is modelled with the Euler equations. The steady Euler solution of the undeformed geometry is then used as the reference

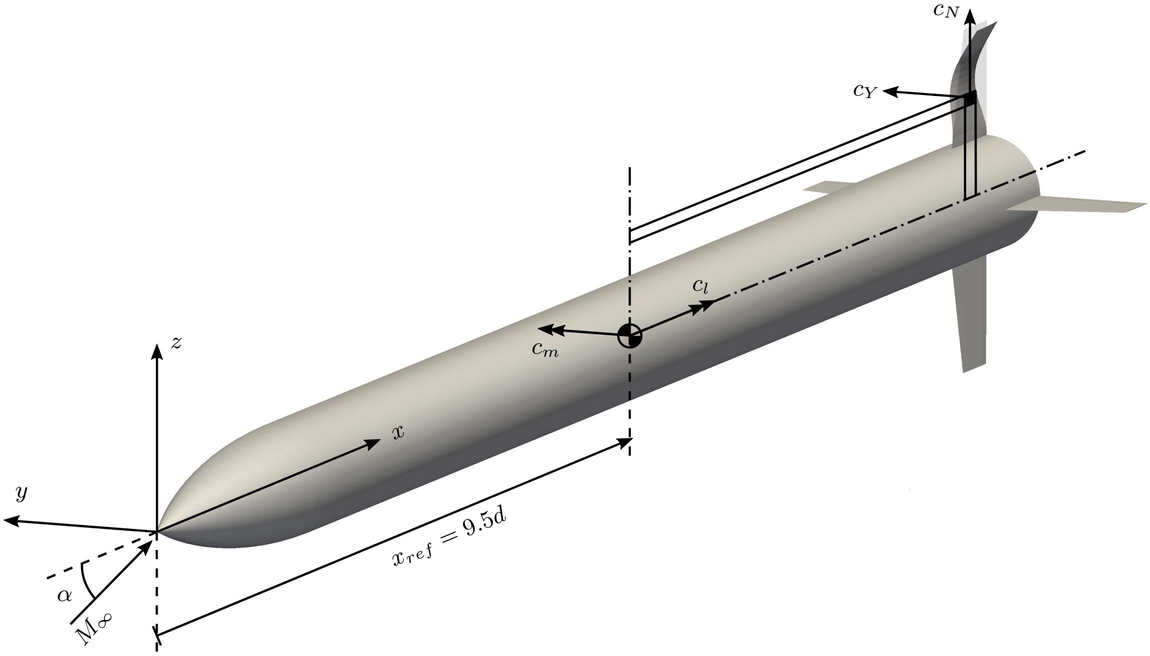

Fig. 4: Nomenclature definition for force coefficients, with the moment reference centre, a wing surface integration element, and mode 3 of the leeside wing shown.

conditions for LPT, with LPT being used to predict the perturbation pressure distribution due to structural deformations. The differences in the integrated force and moment coefficients between the Euler solution and the LPT prediction are then investigated.

1. Euler Solutions

The steady-state Euler equations were solved in OpenFOAM using a solver developed by J. Heyns and O. Oxtoby of the CSIR, South Africa [25]. Solutions using the solver are compared with those obtained in Fluent for the body-alone case in Fig. 5. The solutions of both solvers were determined to be grid-independent through verifying convergence of the integrated loads on three successively refined meshes. Subsequent discussion of Euler solutions in this paper refers to those obtained using OpenFOAM. The sharp change in load-slope in Fig. 5 around $\alpha \approx 8^\circ$ for Mach numbers of $M_\infty = 2.5$ and $M_\infty = 3.0$ is associated with the onset of a crossflow shock on the cylinder. This leads to the development of leeside vortices which provide additional normal force. The shortcomings of using the Euler equations for the physics modelling are shown through comparison to N-S solutions [24] and experimental data [24] for the same geometry, shown in Fig. 6

and Fig. 7. The influence of viscous crossflow drag (largely due to boundary-layer separation and the associated leeside vortex development) on the normal force is seen to be particularly important, with significant differences in the loading and flowfield developing as the angle-of-attack increases. The difference between the Euler and N-S solutions diminishes with the onset of the crossflow shock on the cylinder, as seen for $\alpha \geq 8°$ in Fig. 7.

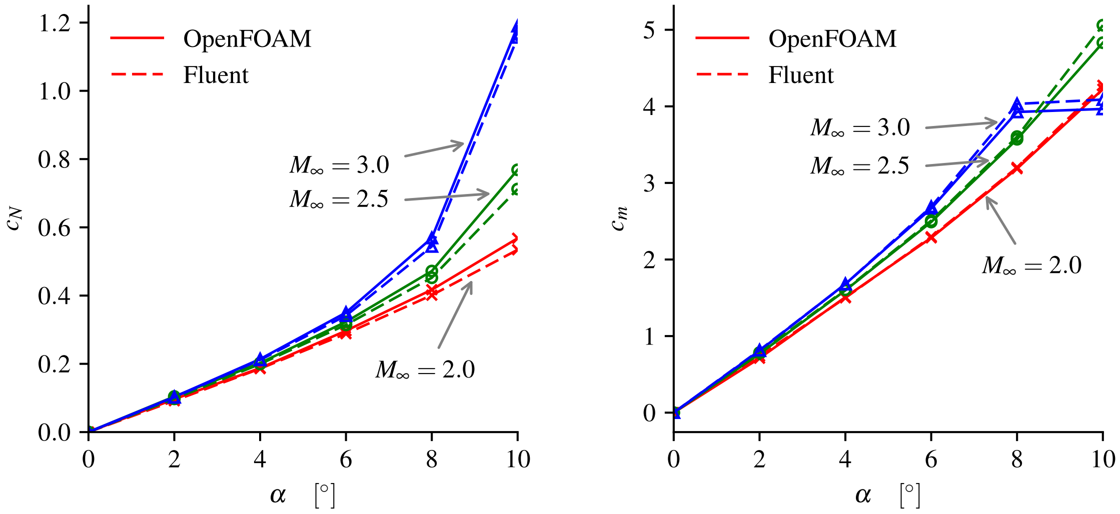

(a)

(b)

Fig. 5: Comparison of Euler-solution body-alone loads by OpenFOAM and Fluent: (a) normal force coefficient, (b) pitching moment coefficient.

2. *Local Piston Theory Perturbations*

In modelling pressure perturbations using piston theory, a variety [26] of pressure equations may be used. Regardless of the order of the pressure equation or the coefficients used, the downwash in LPT is given by

$$w = \mathbf{V}_u \cdot (\hat{\mathbf{n}}_u - \hat{\mathbf{n}}_d) \ , \tag{1}$$

where w is the downwash, $\mathbf{V}_u$ is the local slip velocity on the wing surface, $\hat{\mathbf{n}}_u$ is the unit vector normal to the undeformed wing surface, and $\hat{\mathbf{n}}_d$ is the unit vector normal to the deformed wing surface. (All subsequent terms associated with LPT are evaluated locally at the surface of the wing,

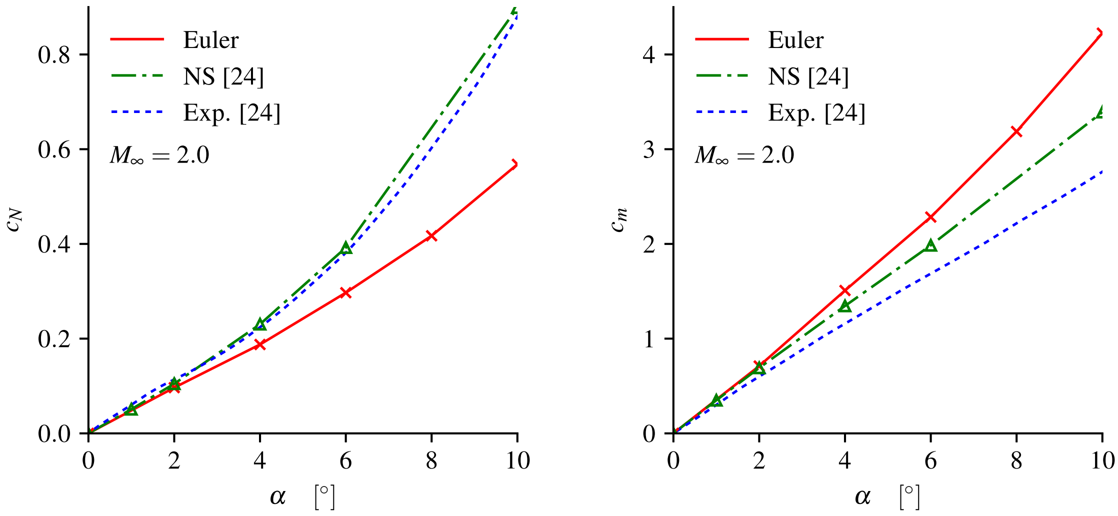

(a)

(b)

Fig. 6: Comparison of body-alone loads by Euler, Navier-Stokes (NS) and experiment (Exp.) at $M_\infty = 2.0$: (a) normal force coefficient, (b) pitching moment coefficient.

with subscript "u" denoting the undeformed wing and subscript "d" denoting the deformed wing. Freestream quantities will be explicitly denoted with the subscript "∞".) The equation for the perturbation pressure is then given [17] by

$$\frac{p_d}{p_u} = 1 + \gamma \left[c_1 \left(\frac{w}{a_u} \right) + c_2 \left(\frac{w}{a_u} \right)^2 + c_3 \left(\frac{w}{a_u} \right)^3 \right] , \tag{2}$$

where p is the fluid pressure, a is the local speed of sound, γ is the ratio of specific heats, and c_i are coefficients from the various pressure equations available [26]. The order of the pressure equation may be truncated to n-th order through setting the coefficients $c_i \equiv 0$ for $i > n$. The coefficients are listed in Table 3 for reference, with M denoting the local Mach number and $m \equiv \sqrt{M^2 - 1}$. Terms associated with the undeformed wing, p_u and a_u, are substituted from a mean-steady solution of the Euler equations.

The variety of coefficients presented in Table 3 reflects the different formulations of piston theory which may be used. The coefficients due to Lighthill's [27], Van Dyke's [28], and Donov [29] have been listed. A thorough treatment of the background of these formulations is outside the scope of the present work, and may be found in [30, 31]. Lighthill's original formulation was based in

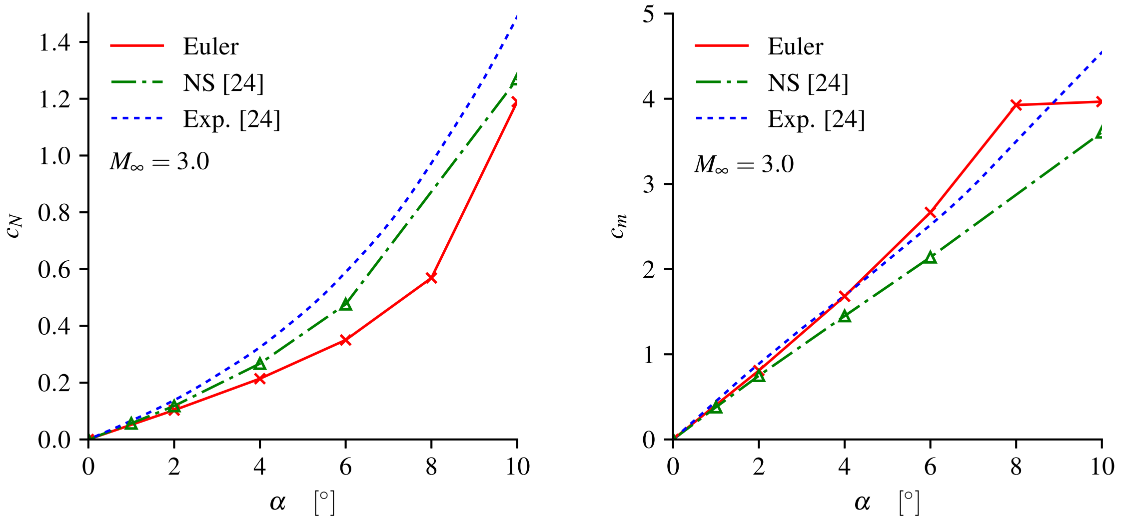

(a) (b)

Fig. 7: Comparison of body-alone loads by Euler, Navier-Stokes (NS) and experiment (Exp.) at $M_\infty = 3.0$: (a) normal force coefficient, (b) pitching moment coefficient.

Table 3: Piston theory coefficients.

Term	Lighthill [27]	Van Dyke [28]	Donov [29]
c_1	1	M/m	M/m
c_2	$(\gamma+1)/4$	$[M^4(\gamma+1) - 4m^2]/4m^4$	$[M^4(\gamma+1) - 4m^2]/4m^4$
c_3	$(\gamma+1)/12$	0	$[8 - 12M^2 + 10(\gamma+1)M^4 + (2\gamma^2 - 7\gamma - 5) + (\gamma+1)M^8]/12Mm^7$

Hayes' [32] hypersonic equivalence principle. It states that hypersonic flow around slender bodies may be considered to occur in independent crossflow planes convected down the body at constant speed. Using this as a conceptual basis, Lighthill [27] postulated that if the resulting downwash Mach number, w/a_u, was subsonic, then the pressure at the surface of the body could be modelled using the equation for a piston producing isentropic waves. A series expansion of the pressure equation led to an expression with the form of Eq. 2 with the coefficients listed in Table 3. Liu et al [26] summarized subsequent developments of piston theory and noted the following assumptions inherent in the works of Lighthill:

$$M_\infty^2 \gg 1, \qquad kM_\infty^2 \gg 1, \qquad k^2M_\infty^2 \gg 1\,, \tag{3}$$

where k is the reduced frequency of unsteady motion of the body. Other aerodynamic methods were found to yield pressure equations with a form similar to Eq. 2. These include the works of Van Dyke [28] and Landahl [33], which are based in a second-order potential flow theory. Also included is the surface-pressure relation for sharp airfoils developed by Donov [29] which was based in the method of characteristics. Liu et al [26] note that the theories of Lighthill, Landahl, and Van Dyke assume that

$$M_\infty\tau \leq 1, \qquad kM_\infty\tau \leq 1\,, \tag{4}$$

where τ is the greater of either the local flow inclination or the airfoil thickness ratio. Donov's method, on the other hand, assumes only that the Mach number is "sufficiently large" and the flow deflection is "sufficiently small" – no rigorous restriction on $M_\infty\tau$, or equivalently w/a_u is made. Finally, the application of piston theory to practical problems in hypersonic flows typically led to its application in flows where the downwash Mach number w/a_u is no longer subsonic. In such flows, it was found that the equation for the pressure behind an oblique shock had a form similar to Eq. 2 in the hypersonic limit. This led to the term "strong-shock piston theory" being applied to this equation. The successful application of piston theory at $w/a_u > 1$ is detailed in [34].

The role of the order of the piston-theory pressure equation and of its coefficients may be illustrated by considering a planar wedge flow, as done in [26, 30]. Differences in the net static force on a wedge are typically only observed between 1st-order and 3rd-order piston theory, as the contribution from 2nd-order terms is symmetrical for the upper and lower surfaces of the airfoil. Nonlinear thickness effects only enter from 3rd-order. Finally, in considering the pressure coefficient on the compression surface, it was noted by [26, 30] that at low downwash-Mach numbers, improved prediction is obtained by using coefficients from Van Dyke [28] or Donov [29] rather than the classical coefficients of Lighthill [27]. At supersonic downwash-Mach numbers, differences between third-order predictions become diminished. However, the predicted pressure becomes unbounded and increased error relative to the exact shock equations is observed. Second-order equations were noted in [26, 30] to have the correct Mach independence as the downwash-Mach number becomes hypersonic.

Euler-based LPT is used in the present work despite the improved fidelity in the mean-steady solution offered by the N-S equations. This is because the theoretical basis of LPT has been established [35] as a special case of the perturbed Euler equations for slender bodies; Euler-based LPT is mathematically consistent. The application of LPT to a mean-steady solution of the N-S equations has not been shown to be mathematically consistent, and has seen varying [18, 19, 36] degrees of success. The change in the aerodynamic loading following structural deformation as obtained from the N-S equations would include not only the influence of the interference flowfield and the local surface inclination, but also the interactions of the viscous boundary-layer. Thus, assessing LPT against the Euler solution offers clearer insight into the role played by the interference flowfield, and establishes a basis for extension of the analysis to viscous solutions.

III. Results and Discussion

The flowfield of the steady Euler solution for the wing-body combination is showed in Fig. 8 and Fig. 9 for $M_\infty = 3.0$, $\alpha = 10°$. From Fig. 8 it is evident that the crossflow shock on the body has developed down the length of the cylindrical portion of the body. This results in the aforementioned symmetrical vortex shedding, which is visualized in Fig. 9. The vertical position of the vortex core is seen to approximately coincide with the semi-span at which maximum displacement occurs for mode 3, as per Fig. 3(b). The integrated loads acting on the leeside wing are shown for a variety of flow conditions and modal displacements in Fig. 10 though Fig. 18. The discussion surrounding these figures will centre on overall load-slope trends for the Euler solutions, the ability of LPT to capture model these trends, the role of the order and coefficients of the pressure equation for LPT, and practical implications relating to cost-reduction for static aeroelasticity. In the course of the discussion, the onset of the crossflow shock and associated body-shed vortices (occurring at approximately $\alpha \geq 10°$ at $M_\infty = 2.5$ and $\alpha \geq 8°$ for $M_\infty = 3.0$) will be referred to regularly, and for brevity will be referred to as “shock onset".

A. Euler Solution of Deformed Geometry

The discussion begins with the load-slope trends of the Euler solution for the deformed geometries. Referring to Fig. 10 through Fig. 15, it is seen that an abrupt change in the load-slopes $\mathrm{d}c_Y/\mathrm{d}\alpha$ and $\mathrm{d}c_m/\mathrm{d}\alpha$ occurs at shock onset. For mode 2, the nature of the change is to increase the magnitude of the slope. Mode 1 exhibits an abrupt change in sign of the load-slopes both for side-force and rolling moment. For mode 3, however, as shown in Fig. 16 through Fig. 18, the slope $\mathrm{d}c_Y/\mathrm{d}\alpha$ is essentially unchanged by the onset of the crossflow shock, while the change in the slope $\mathrm{d}c_m/\mathrm{d}\alpha$ for mode 3 is one of gradual sign reversal. These trends are observed for both mode deflection magnitudes.

The gradual $\mathrm{d}c_m/\mathrm{d}\alpha$ slope reversal observed for mode 3 is related to an interaction between the progression of the vortex-core position down the wing span with increasing angle-of-attack and the normal-vector distribution of the mode-shape (which is the main mechanism of side-force, and by extension, rolling-moment production). This is evident from the difference in the slope trend of $\mathrm{d}c_Y/\mathrm{d}\alpha$ and $\mathrm{d}c_m/\mathrm{d}\alpha$ following shock onset, which highlights the movement of the spanwise position of the wing centre-of-pressure. In contrast, the similarity between the force and moment slopes observed for modes 1 and 2, as per Fig. 10 through Fig. 15, suggests the centre-of-pressure is not significantly influenced by shock onset for these modes. Regarding the role of displacement magnitude, it is noted that for all the cases considered, a linear scaling of the loads is observed with displacement.

B. Load-Slope Prediction Accuracy of Local Piston Theory

The ability of LPT to replicate the load-slope trends obtained by the Euler solution of the deformed geometry is now considered. It is found that notable differences between the load magnitudes predicted by the various pressure-equation orders and pressure-equation coefficients may be observed, while the variation in load-slope between models is insignificant. This results in effective prediction “bands" for the loads. In this subsection, the slope trends of LPT prediction bands are discussed as a group; a discussion of the individual curves is reserved for the following subsection.

In discussing the differences in trends between modes, it is of importance to note the difference in the magnitude of the loads. The loads of mode 2, as per Fig. 13 through Fig. 15, are seen to be an order of magnitude larger than those of mode 1, in Fig. 10 through Fig. 12, and mode 3, per Fig. 16 through Fig. 18. This is related to the difference in side-force production mechanism between the modes. Mode 2 is the first torsion mode and, as seen from Fig. 3(a), exhibits almost no bending down the mid-chord. Modal displacement translates directly to a change in inclination of the local chord to the oncoming flow, and so, for the large displacements considered, the loading is dominated by the surface displacement while the influence of the leeside vortices is of secondary importance. This may be seen in Fig. 13 through Fig. 15 by considering the ratio of load magnitude before to after shock onset – the relative sensitivity of the loading to shock onset is seen to be much smaller in the case of mode 2 compared to modes 1 and 3. Conversely, it is seen that the loading in the case of mode 1 (which per Fig. 2(b) is the first-bending mode with little torsion) and of mode 3 (as per Fig. 3(b), the second bending mode, with chordwise deformation along the mid-span) is much more strongly influenced by the leeside vortices. This is because the mode-shapes do not exhibit significant torsion (and the associated inclination of the local chord to the flow).

It is therefore not surprising that LPT is seen to capture the load-slopes of mode 2 significantly better than it does for modes 1 and 3. LPT is inherently a surface-local, inclination-based method, and does not model interactions with the surrounding flowfield as the surface displaces. The increase in differences between the LPT load-slopes and Euler load-slopes that is noted with increasing M_∞ (and by extension, increasing vortex strength) and δ (resulting in the surface being displaced closer to the vortex core), are thus to be expected.

A further point of interest is the difference in low-α slope prediction accuracy for modes 1 and 3. In particular, we consider the case of $M_\infty = 2.0$, with no shock onset and vortex development. We note in Fig. 10 that for mode 1, good prediction in the load slope is achieved for low angles-of-attack, for $\alpha \leq 6°$, for both displacement magnitudes. For mode 3, however, Fig. 16 shows a near-constant (with α) offset in the load slope, which scales linearly with displacement magnitude. Differences between the LPT slopes and the Euler load-slopes are due to interaction with the entropy wake from the nose-shock in the flowfield near the wings. The differences noted in the load-slopes between mode 1 and mode 3 are related to the geometric differences of the mode-shapes.

Finally, the failure of LPT to capture the $\mathrm{d}c_Y/\mathrm{d}\alpha$ slope for mode 3 at $M_\infty = 3.0$ following shock onset, depicted in Fig. 18, suggests a more prominent interaction with the vortex than in the case of the other modes considered. This is likely due to the coincidence of the vortex core position with the position of maximum modal displacement.

C. Influence of Local Piston Theory Order and Coefficients

As a foreword to the discussion on the role of the order of pressure equation and its coefficients, the geometric differences between the mode-shapes and the difference in load magnitudes are considered. Referring to the downwash equation, Eq. 1, it is noted that the downwash magnitude is directly related to the turning of the local velocity vector as enforced by modal displacement. This in turn enters the pressure equation, Eq. 2, as a downwash Mach number, w/a_u. It has previously been remarked that modes 1 and 3 are predominantly pure-bending modes, with mode 3 exhibiting a degree of chordwise deformation at the maximum-displacement span station. Bending – which is essentially translation of the chord normal to the thickness plane – does not induce significant rotation of the surface normal-vector into the mean steady flow velocity. This results in a small downwash-Mach for mode 1. The chordwise deformation of mode 3 results in somewhat higher downwash-Mach numbers locally, as the normal vectors are inclined into the mean flow vector, but the overall effect is marginal. The torsion of mode 2, on the other hand, results in significantly larger inclination of the surface normal-vector into the mean flow, and in the case of $\delta = 10\,\mathrm{mm}$, the downwash-Mach numbers on the wing surface are $w/a_u \approx 1$. In this sense, mode 2 produces large perturbations, while modes 1 and 3 produce small perturbations even for large displacements.

Turning to the results in Fig. 10 through Fig. 18, it is noted that the loads predicted using Lighthill's coefficients are consistently smaller than those obtained using Van Dyke's or Donov's coefficients. Two further trends are noted from the data for modes 1 and 3, which are supported by the observations in [26, 30]: (1) the difference between the 3rd-order predictions of Van Dyke and Donov are indistinguishable; (2) the loads from 1st-order and 2nd-order equations of the same source are identical. In the case of particularly low downwash-Mach numbers, as associated with mode 1 and $\delta = 5\,\mathrm{mm}$ for mode 3, it is noted that the contribution from the 3rd-order terms is negligible, and the curves for all three orders collapse to a single curve described by the 1st-order equation.

In the case of mode 1, better load prediction at low angle-of-attack is obtained by using Van Dyke's coefficients than by Lighthill's coefficients. However, the difference is marginal and significant deviation from the Euler solution occurs as interaction with the flowfield increases. As previously noted, flowfield interaction is particularly prominent for mode 3, and poor prediction is obtained regardless of the coefficients chosen. For the larger displacement of $\delta = 10\,\mathrm{mm}$ for mode 3, a slight difference between the 2nd-order and the 3rd-order contributions is noted, with the difference increasing with the freestream Mach number.

Considering the case of large downwash-Mach numbers associated with mode 2, shown in Fig. 13 through Fig. 15, it is noted that the choice of coefficients and equation order becomes significant. Here, a difference between the 1st-order and the 2nd-order loads is observed. This is due to the 2nd-order contribution no longer being symmetrical with respect to thickness, as expansion to vacuum pressure occurs on the suction surface. This is observed to occur only for the larger displacement of $\delta = 10\,\mathrm{mm}$. It is noted that for the large downwash-Mach number, the best correlation with the Euler-solution loads is obtained using a 2nd-order pressure equation. The 1st-order equation under-predicts the loads, while the 3rd-order equation progressively over-predicts loads as M_∞ increases. This is in agreement with the 2nd-order equation being the only formulation to adhere to the Mach-independence principle, as noted in [26, 30]. Finally, it is noted that for mode 2, better prediction is obtained by using Lighthill's coefficients than by Van Dyke's coefficients.

D. Implications for Local Piston Theory Application

The discussion closes by noting that the accuracy of LPT load-slope prediction deteriorated for mode-shapes which did not induce significant static loads, such as bending modes. In these cases, the interaction of the structural displacement with the surrounding flowfield could not be neglected, as is done with LPT. However, accurate predictions were obtained by LPT for cases for which the displacement field has a high aerodynamic stiffness. This was noted even under large deformations.

The results of the present investigation highlight both the successes and limitations of LPT in aerodynamically-interfering flows. LPT gives useful prediction of load-slopes when the perturbation loading is dominated by changes in the local inclination of the surface. This was demonstrated by the good correlation with full Euler solutions obtained for the first torsion mode (Mode 2).

In contrast, the bending modes (Modes 1 and 3) gave notably poorer correlation of load-slopes with the Euler solutions. This is an indication that the aerodynamic stiffness for these cases is dominated by interaction between the structural displacement and the body-shed vortices. This demonstrates the shortcomings of LPT in modelling perturbations which are dominated by interaction with surrounding flow features. Examples of such flows include the moderate- and strong-interaction regime for boundary layers, corner-flows, or strong interaction of control surfaces with impinging vortices. With the LPT shortcomings already present within the mathematically-consistent framework of inviscid flow, it cannot be expected that a Navier-Stokes-based LPT will offer significant improvement in prediction. The extension of LPT to account for flowfield interaction remains an area for future work.

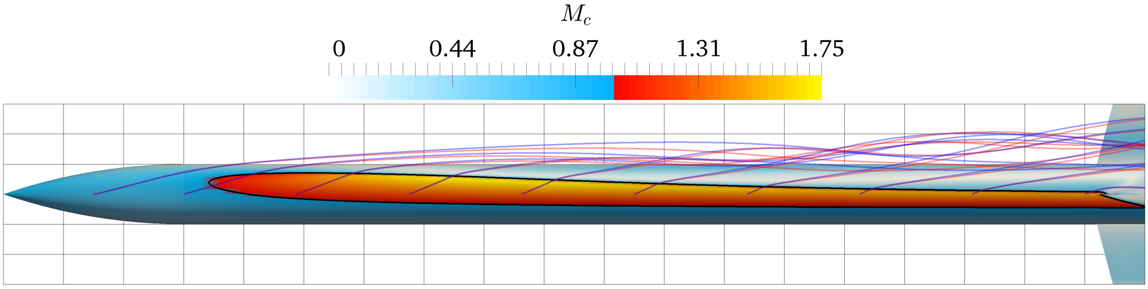

Fig. 8: Flowfield and crossflow Mach number (M_c) distribution at $M_\infty = 3$, $\alpha = 10°$; contour of $M_c = 1$.

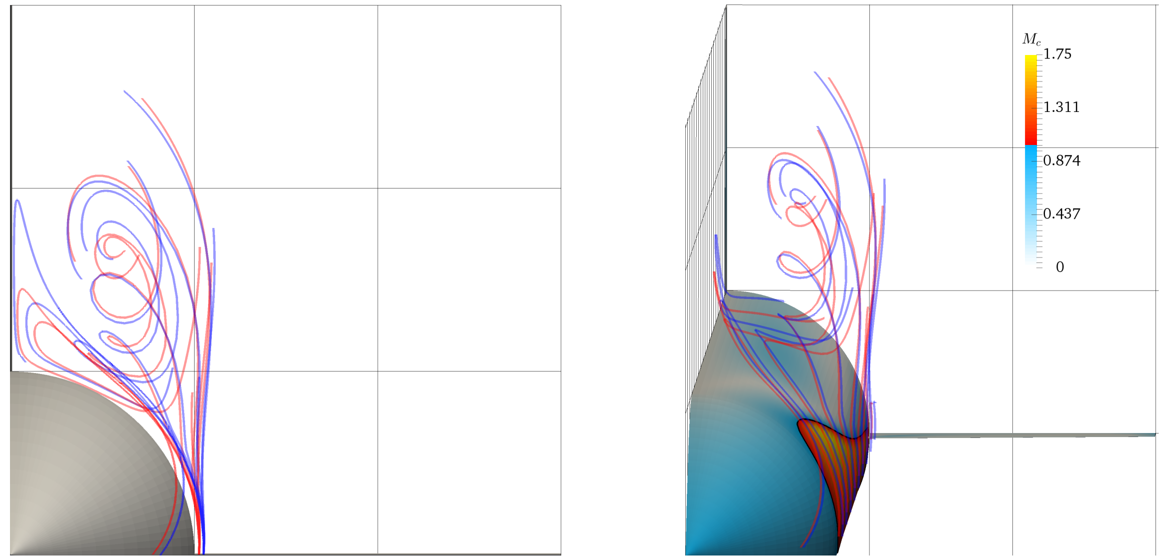

(a) (b)

Fig. 9: Body-vortex structure at $M_\infty = 3$, $\alpha = 10^\circ$ viewed: (a) from the nose, (b) with crossflow Mach number (M_c) distribution; contour of $M_c = 1$.

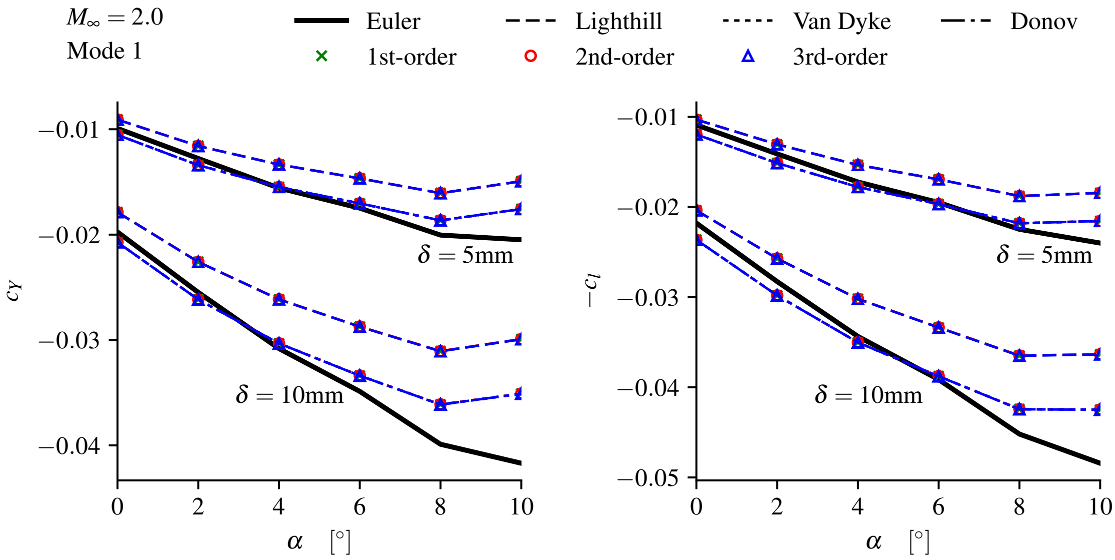

Fig. 10: Side-force coefficient and rolling-moment coefficient contribution from the leeside wing: comparison of Euler and LPT, mode 1 (first bending), $M_\infty = 2.0$.

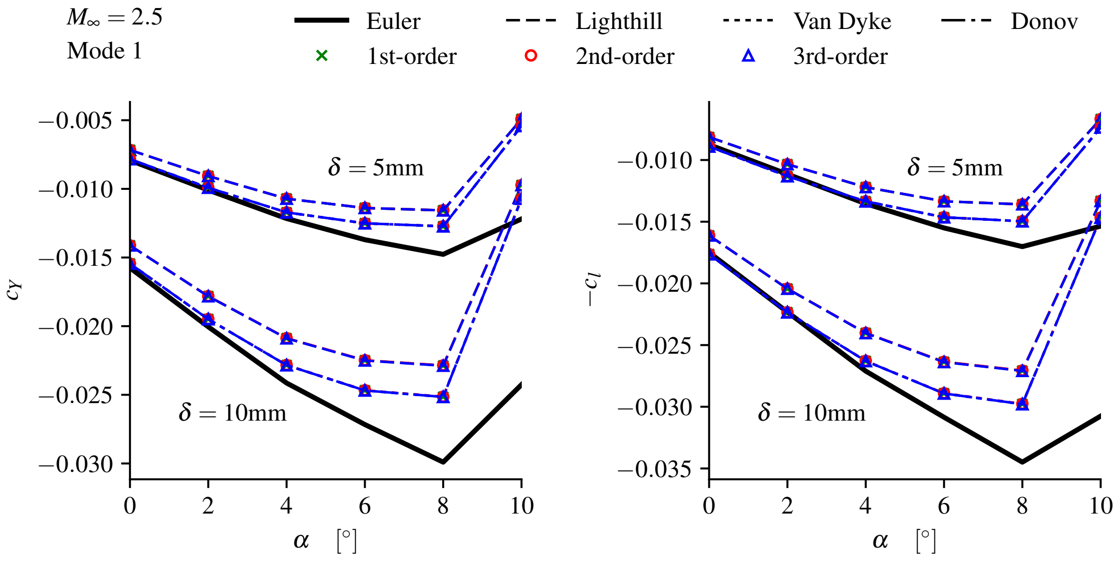

Fig. 11: Side-force coefficient and rolling-moment coefficient contribution from the leeside wing: comparison of Euler and LPT, mode 1, $M_\infty = 2.5$.

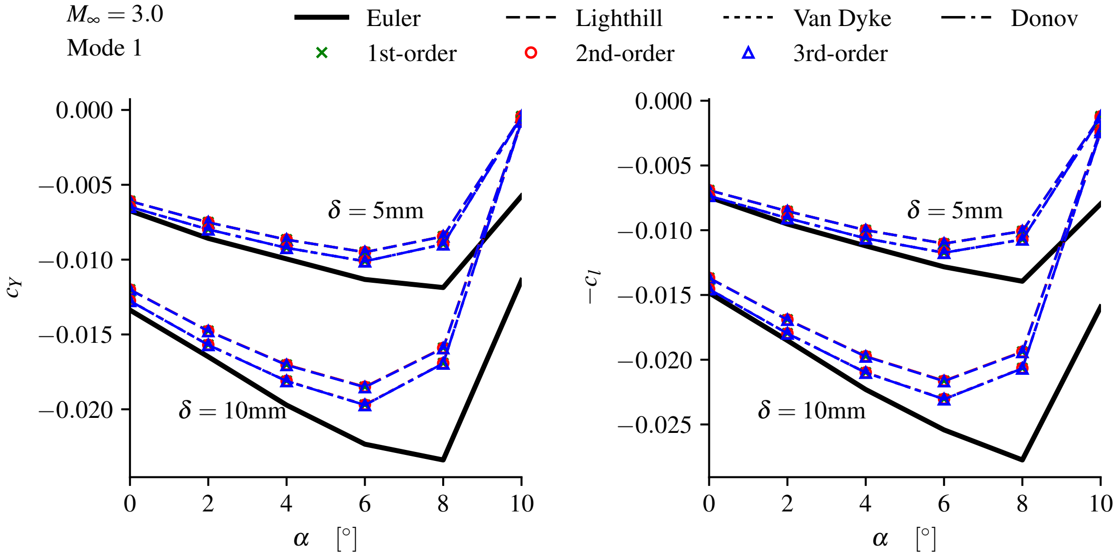

Fig. 12: Side-force coefficient and rolling-moment coefficient contribution from the leeside wing: comparison of Euler and LPT, mode 1 (first bending), $M_\infty = 3.0$.

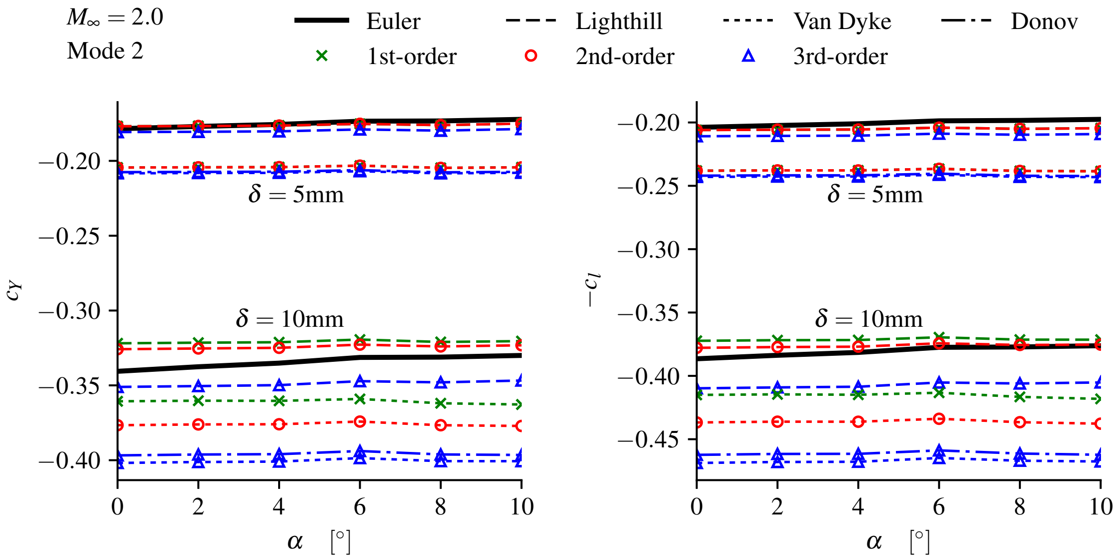

Fig. 13: Side-force coefficient and rolling-moment coefficient contribution from the leeside wing: comparison of Euler and LPT, mode 2 (first torsion), $M_\infty = 2.0$.

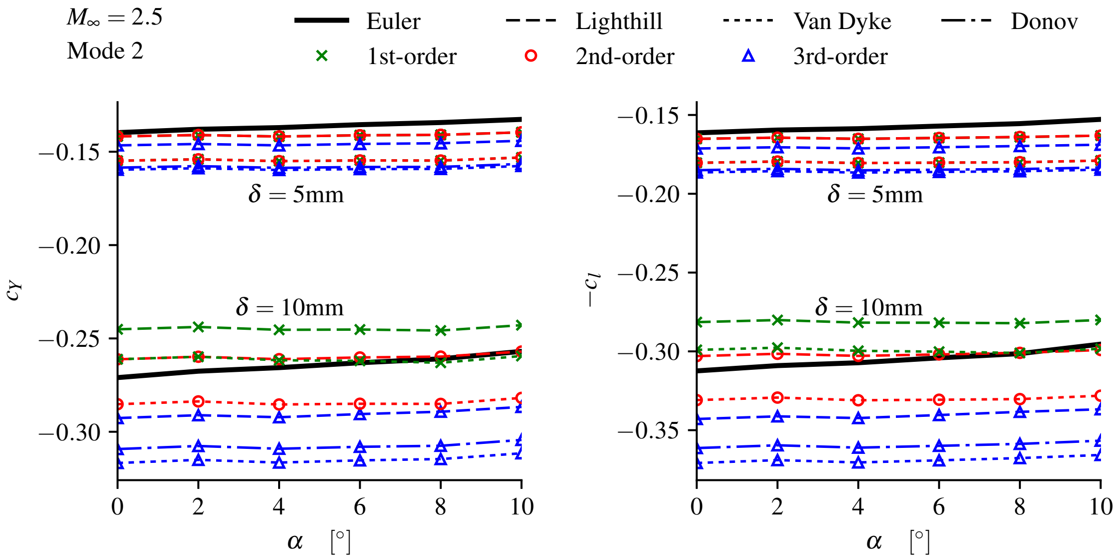

Fig. 14: Side-force coefficient and rolling-moment coefficient contribution from the leeside wing: comparison of Euler and LPT, mode 2 (first torsion), $M_\infty = 2.5$.

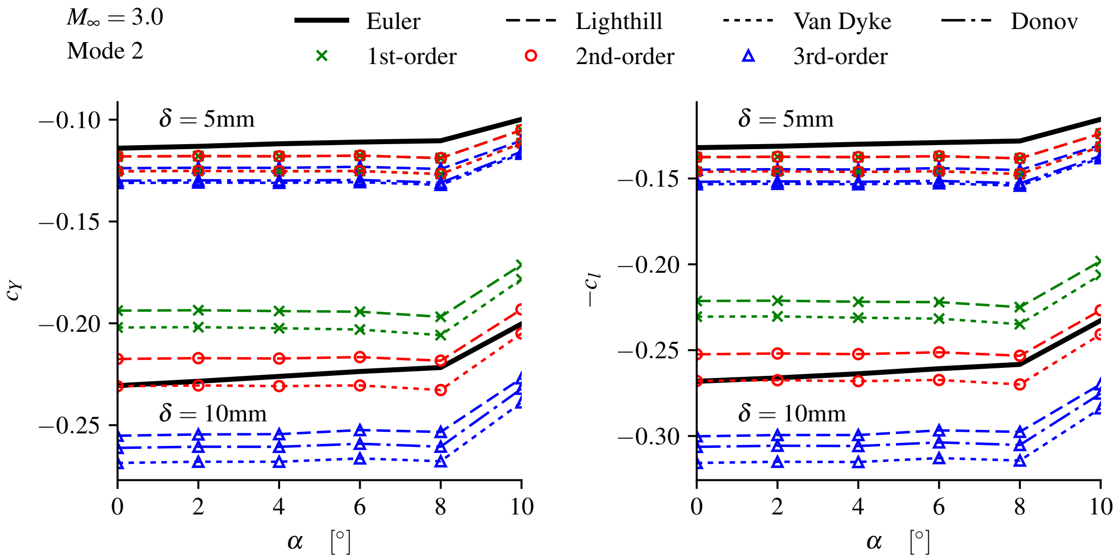

Fig. 15: Side-force coefficient and rolling-moment coefficient contribution from the leeside wing: comparison of Euler and LPT, mode 2 (first torsion), $M_\infty = 3.0$.

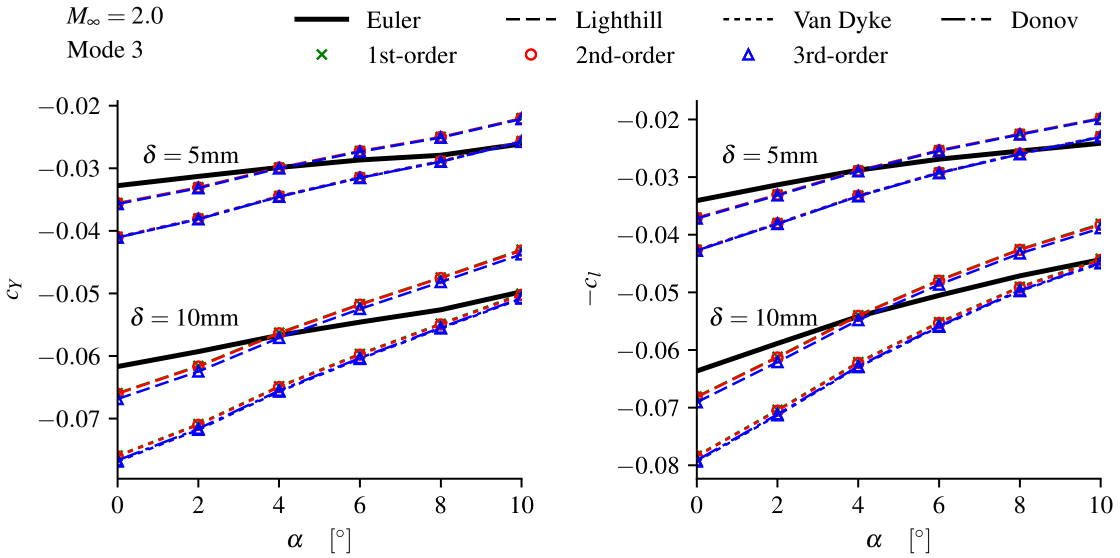

Fig. 16: Side-force coefficient and rolling-moment coefficient contribution from the leeside wing: comparison of Euler and LPT, mode 3 (second bending), $M_\infty = 2.0$.

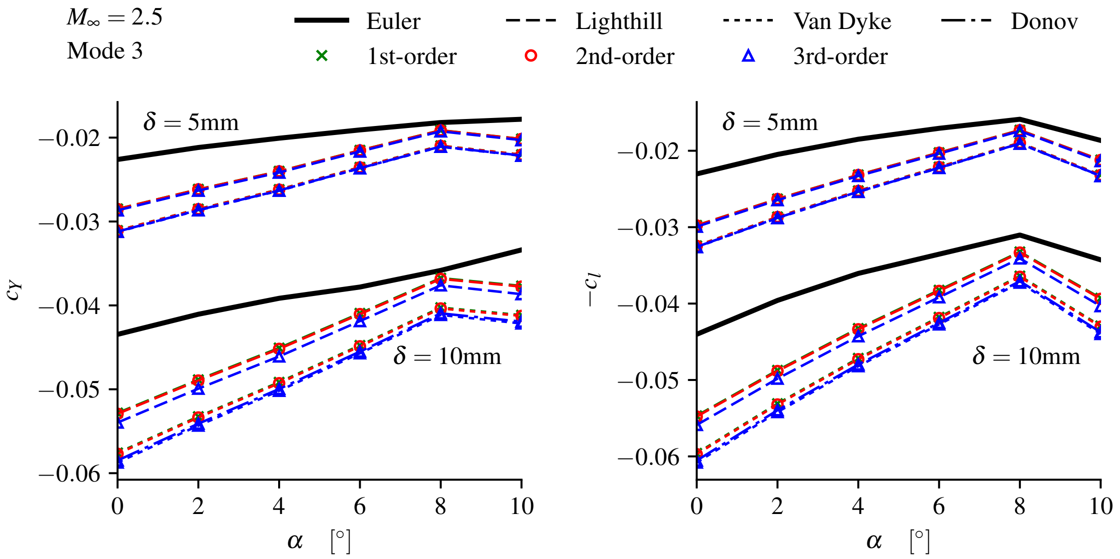

Fig. 17: Side-force coefficient and rolling-moment coefficient contribution from the leeside wing: comparison of Euler and LPT, mode 3 (second bending), $M_\infty = 2.5$.

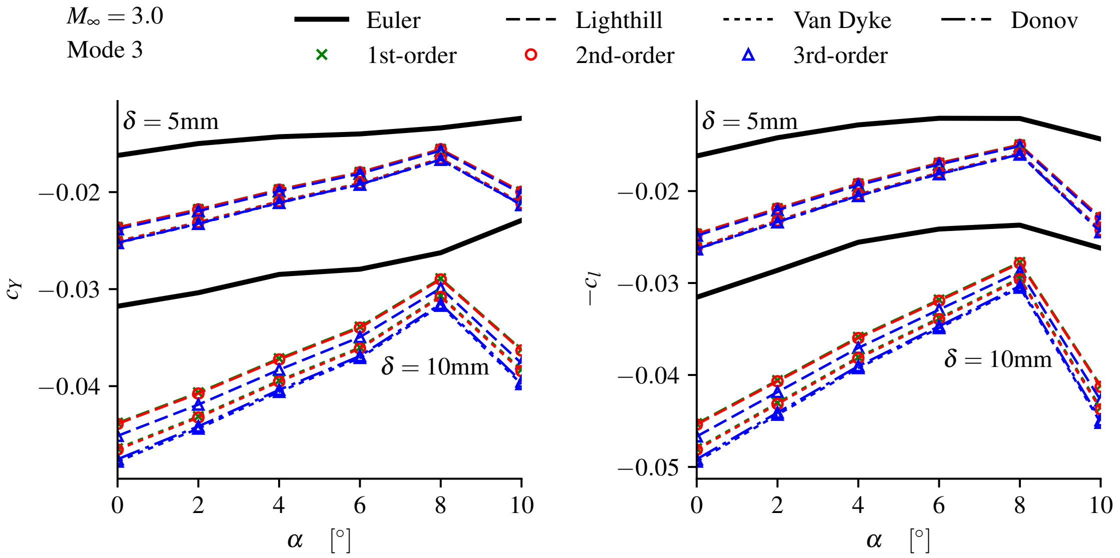

Fig. 18: Side-force coefficient and rolling-moment coefficient contribution from the leeside wing: comparison of Euler and LPT, mode 3 (second bending), $M_\infty = 3.0$.

IV. Conclusions

In the present work, LPT has been applied to a wing-like structure subject to aerodynamic interference to determine the suitability of LPT in modelling static loads in an interfering flowfield. It has been shown that good correspondence with Euler solutions in the load-slope may be attained in the parameter space investigated, provided that the loads on the surface are dominated by non-interference effects such as local twisting of the wing. This has been found even for large deformations in which the perturbation downwash-Mach number is of the order of 1. However, when in applications where the loading is dominated by interference with the surrounding flowfield, such as interaction with vortices shed from upstream of the wing, the load-slope prediction accuracy of LPT was seen to deteriorate as expected, while still providing useful prediction.

The influence of the pressure equation order and the coefficients used was also investigated. It was found that 1st-order LPT is sufficient in cases where surface deflection produce small perturbations, as quantified by the downwash-Mach number. In the case of large downwash-Mach numbers, the use of 2nd-order LPT is recommended. The choice between classical piston theory coefficients from [27] or those from the second-order theory of [28] has not been shown to have a significant influence on the load prediction accuracy.

The cost reduction relative to mesh deformation offered by LPT suggests that it is a useful alternative in predicted perturbation loads and determining aerodynamic stiffness of torsion-dominant modes.

References

[1] Yates, E. and Bland, S., "Comparative Evaluation of Methods for Predicting Flutter and Divergence of Unswept Wings of Finite Span," NASA TN D-2051, NASA, Washington, DC, 1963.

[2] Anderson, J., *Fundamentals of Aerodynamics*, McGraw-Hill Education, 6th ed., 2016.

[3] Albano, E. and Rodden, W., "A doublet-lattice method for calculating lift distributions on oscillating surfaces in subsonic flows," *AIAA Journal*, Vol. 7, No. 2, 1969, pp. 279–285.

[4] Appa, K., "Constant pressure panel method for supersonic unsteady airload analysis," *Journal of Aircraft*, Vol. 24, No. 10, 1987, pp. 696–702.

[5] Zhang, W.-W., Ye, Z.-Y., Zhang, C.-A., and Liu, F., "Supersonic flutter analysis based on a local piston theory," *AIAA Journal*, Vol. 47, No. 10, 2009, pp. 2321–2328.

[6] Yao, W. and Marques, S., "Nonlinear aerodynamic and aeroelastic model reduction using a discrete empirical interpolation method," *AIAA Journal*, Vol. 55, No. 2, 2017, pp. 624–637.

[7] Thomas, J., Dowell, E., and Kenneth, C., "Three-dimensional transonic aeroelasticity using proper orthogonal decomposition-based reduced-order models," *Journal of Aircraft*, Vol. 40, No. 3, 2003, pp. 554–551.

[8] Crowell, A., McNamara, J., and Miller, B., "Hypersonic aerothermoelastic response prediction of skin panels using computational fluid dynamic surrogates," *Journal of Aeroelasticity and Structural Dynamics*, Vol. 2, No. 2, 2011, pp. 3–30.

[9] Statnikov, V., Meinke, M., and Schröder, W., "Reduced-order analysis of buffet flow of space launchers," *Journal of Fluid Mechanics*, Vol. 815, 2017, pp. 1–25.

[10] Chinesta, F., Keunings, R., and Leygue, A., *The proper generalized decomposition for advanced numerical simulations: a primer*, Springer International Publishing, 2014.

[11] Badías, A., González, D., Alfara, I., Chinesta, F., and Cueto, E., "Local proper generalized decomposition," *International Journal for Numerical Methods in Engineering*, pp. 1–21.

[12] Bendiksen, O., "Review of unsteady transonic aerodynamics: theory and applications," *Progress in Aerospace Sciences*, Vol. 47, 2011, pp. 135–167.

[13] Hayes, W. and Probstein, R., *Hypersonic flow theory: inviscid flows*, Vol. 1, Academic Press, 2nd ed., 1966.

[14] Tannehill, J., Anderson, D., and Platcher, R., *Computational fluid mechanics and heat transfer*, Taylor & Francis, 2nd ed., 1997.

[15] Cowan, T., O'Neill, C., and Arena, A., "Transpiration boundary condition for computational fluid dynamics solutions in noninertial reference frames," *Journal of Aircraft*, Vol. 41, No. 5, 2004, pp. 1252–1255.

[16] Da Ronch, A., Ghoreyshi, M., Vallespin, D., Badcock, K., Mengmeng, Z., Oppelstrup, J., and Rizzi, A., "A framework for constrained control allocation using CFD-based tabular data," in "49th AIAA Aerospace Scineces Meeting including the New Horizons Forum and Aerospace Exposition," Orlando, Florida, 2011.

[17] Meijer, M.-C. and Dala, L., "Zeroth-order flutter prediction for cantilevered plates in supersonic flow," *Journal of Fluids and Structures*, Vol. 57, 2015, pp. 196–205.

[18] McNamara, J., Crowell, A., Friedmann, P., Glaz, B., and Gogulapati, A., "Approximate modeling of

unsteady aerodynamics for hypersonic aeroelasticity," *Journal of Aircraft*, Vol. 47, No. 6, 2010, pp. 1932–1945.

[19] Liu, W., Zhang, C.-A., Han, H.-Q., and Wang, F.-M., "Local piston theory with viscous correction and its application," *AIAA Journal*, Vol. 55, No. 3, 2017, pp. 942–954.

[20] Hunter, J., *An efficient method for time-marching supersonic flutter predictions using CFD*, Master's thesis, Oklahoma State University, Stillwater, Oklahoma, 1997.

[21] Brouwer, K., Crowell, A., and McNamara, J., "Rapid prediction of unsteady aeroelastic loads in shock-dominated flows," in "56th AIAA/ASCE/AHS/ASC Structures, Structural Dynamics, and Materials Conference, AIAA SciTech Forum," Kissimmee, Florida, 2015.

[22] Shi, X., Tang, G., Yang, B., and Li, H., "Supersonic flutter analysis of vehicles at incidence based on local piston theory," *Journal of Aircraft*, Vol. 49, No. 1, 2012, pp. 333–337.

[23] Zhang, Q., Ye, K., Ye, Z.-Y., and Zhang, W.-W., "Approximate modeling of unsteady aerodynamics for hypersonic aeroelasticity," *Journal of Aircraft*, Vol. 53, No. 4, 2016, pp. 1065–1072.

[24] Tuling, S., *An engineering method for modeling the interaction of circular bodies and very low aspect ratio cruciform wings at supersonic speeds*, Ph.D. thesis, University of West England, Bristol, United Kingdom, 2013.

[25] Heyns, J. and Oxtoby, O., "Modelling external high-speed aerodynamics," in "5th OpenFOAM User Conference," Weisbaden, Germany, 2017.

[26] Liu, D., Yao, Z., Sarhaddi, D., and Chavez, F., "From piston theory to a unified hypersonic-supersonic lifting surface method," *Journal of Aircraft*, Vol. 34, No. 3, 1997, pp. 304–312.

[27] Lighthill, M., "Oscillating airfoils at high Mach numbers," *Journal of the Aeronautical Sciences*, Vol. 20, No. 6, 1953, pp. 402–406.

[28] Van Dyke, M., "A study of second-order supersonic flow theory," NACA Report 1081, Washington, DC, 1952.

[29] Donov, A., "A flat wing with sharp edges in a supersonic stream," NACA TM-1394, Washington, DC, 1956.

[30] Meijer, M.-C. and Dala, L., "Generalized formulation and review of piston theory for airfoils," *AIAA Journal*, Vol. 54, No. 1, 2016, pp. 17–27.

[31] Meijer, M.-C. and Dala, L., "Quantifying non-linearity in planar supersonic potential flows," *The Aeronautical Journal*, Vol. 121, No. 1237, 2017, pp. 372–394.

[32] Hayes, W., "On hypersonic similitude," *Quarterly of Applied Mathematics*, Vol. 5, No. 1.

[33] Ashley, H. and Zartarian, G., "Unsteady Flow Around Thin Wings at High Mach Number," *Journal of*

the Aeronautical Sciences, Vol. 24, No. 1, 1957, pp. 33–38, url =.

[34] Raymond, J., "Piston theory applied to strong shocks and unsteady flow," *Journal of Fluid Mechanics*, Vol. 8, No. 4, 1960, pp. 509–513, url =.

[35] Meijer, M.-C., "Piston theory applied to wing-body configurations: a review of the mathematical basis," in "Research and Education in Aircraft Design," Warsaw, Poland, 2016.

[36] Crowell, A., *Model reduction of computational aerothermodynamics for multi-discipline analysis in high speed flows*, Ph.D. thesis, Ohio State University, Columbus, Ohio, 2013.